Journal of Computational Physics **161,** 379–400 (2000)
doi:10.1006/jcph.2000.6460, available online at http://www.idealibrary.com on IDEAL®

Comparison between Staggered and Unstaggered Finite-Difference Time-Domain Grids for Few-Cycle Temporal Optical Soliton Propagation

L. Gilles,*,† S. C. Hagness,* and L. Vázquez†

*Department of Electrical and Computer Engineering, University of Wisconsin, 1415 Engineering Drive, Madison, Wisconsin 53706; and †Departamento de Matemática Aplicada, Escuela Superior de Informática, Universidad Complutense, E-28040 Madrid, Spain
E-mail: lgilles@lyra.ece.wisc.edu and hagness@engr.wisc.edu

Received July 21, 1999; revised January 19, 2000

The auxiliary-differential-equation formulation of the finite-difference time-domain method has become a powerful tool for modeling electromagnetic wave propagation in linear and nonlinear dispersive media. In the first part of this paper, we compare the stability and accuracy of second- and fourth-order-accurate spatial central discretizations on staggered grids with a third-order-accurate spatial discretization on an unstaggered grid, combined with a second-order leapfrog time integration scheme for modeling linear dispersive phenomena in a one-dimensional single-resonance Lorentz medium. We use on the unstaggered grid the NS2 scheme introduced by Y. Liu, which combines forward and backward differencing for the spatial derivatives. Phase and attenuation errors are determined analytically across the entire frequency band of the low-loss single-resonance Lorentz model. In the second part of the paper, we compare the use of one-dimensional staggered and unstaggered grids for modeling the transient evolution of few-cycle optical localized pulses in a dispersive Lorentz medium with a delayed third-order nonlinearity. The focus of the study is on the decay of higher-order solitons under the combined action of dispersion, self-phase modulation, self-steepening, and stimulated Raman scattering. Numerical results from the simulations on the unstaggered and staggered grids are in excellent agreement. This study demonstrates the accuracy of the unstaggered scheme augmented with a linear/nonlinear dispersive media formulation for temporal soliton propagation.

Key Words: finite-difference time-domain methods; Maxwell's equations; staggered grids; unstaggered grids; material dispersion; nonlinear optics; optical solitons.

1. INTRODUCTION

Finite-difference time-domain (FDTD) modeling of electromagnetic pulse propagation in nonlinear optical materials has recently gained much attention [1]. The auxiliary-differential-equation (ADE) formulation, initially developed for linear dispersive materials [2], is currently the most commonly used approach for incorporating the nonlinear relationship between the polarization vector and the electric field into the FDTD Maxwell's equation solver [3, 4]. This modeling capability has been applied to a variety of second- and third-order nonlinear phenomena, including temporal and spatial soliton propagation [3, 5, 6], self-focusing of optical beams [4], scattering from linear–nonlinear interfaces [7], pulse propagation through nonlinear corrugated waveguides [8], pulse-selective behavior in nonlinear Fabry–Perot cavities [9], and second-harmonic generation in nonlinear waveguides [10].

Stability, numerical dispersion, and artificial dissipation are factors in FDTD-ADE modeling that must be accounted for to understand the algorithm's operation and its accuracy limits. Petropoulos [11], Young *et al.* [12], and Cummer [13] have analyzed the stability and numerical dispersion relations for second-order-accurate central differencing schemes involving the Yee [14] staggered grid where the electric and magnetic field vectors are interleaved. Using a different approach, Petropoulos [15] determined the grid resolution, in terms of a fixed total computation time and desired phase error, for both second- and fourth-order Yee schemes in two dimensions for free-space propagation.

In the past, staggered grids have usually been preferred over unstaggered grids for the following reasons. On an unstaggered grid, the electric and magnetic field vectors are placed on the same primary grid and all vector field components are colocated. Central differencing on an unstaggered grid can lead to undesirable numerical oscillations due to odd–even decoupling [16]. Moreover, the standard unstaggered scheme produces a relative total numerical phase velocity error four times greater than the staggered scheme due to the wider stencil. Despite these problems, the unstaggered grid with its inherently colocated electric field vector components offers several advantages specific to the modeling of optical wave phenomena. For example, unstaggered schemes enable the use of a moving window coordinate frame for tracking long-distance optical pulse propagation [17, 18]. Most importantly, the use of a grid with colocated electric field vector components is essential for efficient and accurate modeling of nonlinear optical wave propagation in two or three dimensions. The reason for this is the fact that the presence of the nonlinearity requires calculating higher-order powers of the electric field intensity at a given point in space at every time step. If the electric field vector components are not colocated, as is the case with the staggered Yee scheme, then the field intensity at a given point in space must be interpolated from the known field components centered around that point. This interpolation is costly in terms of computational efficiency and accuracy, and can be avoided altogether if the electric field vectors are colocated.[1]

Liu [19] suggested an interesting way to combine the desirable properties of the staggered and unstaggered grids. His approach uses noncentral differencing based on a combination

[1] We note that the unstaggered grid is not the only option for colocating the electric field vector components. For example, colocated staggered grids have been proposed where the electric and magnetic field vectors are placed on dual grids but where all components of any given field vector are colocated [19]. We do not consider those schemes here because they require about twice the number of operations [19]. Furthermore, a 1D version of such a scheme does not exist.

of forward and backward differencing (FD/BD) for the spatial derivatives on an unstaggered grid. In this manner, the even–odd coupling is preserved even though the fields are colocated; thus spurious oscillations are avoided. The methods referred to as NS2 and NS3 in [19] (NS meaning "nonsymmetric") are finite-difference (FD) discretizations of first-order derivatives in Maxwell's curl equations with third- and first-order accuracy, respectively. In [19], numerical experiments supported the claim that the NS2 and NS3 schemes targeted fourth- and sixth-order accuracy in space, respectively, as is the case for the corresponding wave-equation systems containing second-order derivatives. However, as shown recently by Driscoll and Fornberg [20], such noncentral differencing only retains the accuracy of the first-order derivatives.

In this paper, we compare the Yee (staggered) and Liu NS2 (unstaggered) schemes for modeling pulse propagation in linear and nonlinear dispersive media. Time integration is performed for both grid configurations in the usual second-order leapfrog manner. Second- and fourth-order spatial accuracy is considered on the staggered grids and third-order spatial accuracy on the unstaggered grid. Therefore, we denote the various schemes as Y22, Y24, and NS2. We do not include the NS3 method in this analysis as it is only first-order accurate and therefore unable to capture the correct physics in the medium absorption band.

First, we compare the stability and accuracy of the Y22, Y24, and NS2 FDTD-ADE schemes for a *linear* single-resonance Lorentz medium. We conduct a Von Neumann analysis of each approach in order to determine stability criteria. Using CFL numbers below and at the stability limit, we investigate phase and attenuation errors across the entire frequency band of the Lorentz model. Second, we compare the results from the two grid arrangements in modeling the transient evolution of few-cycle optical localized pulses in a Lorentz dispersive medium with *nonlinear* third-order delayed response modeling Raman scattering. Since the Courant limit for the nonlinear algorithm is not known, the nonlinear algorithms were run below their linear CFL limit.

The focus of the numerical experiments is on the decay of linearly polarized fundamental and second-order bright soliton pulses due to the combined action third-order dispersion (TOD), self-phase modulation (SPM), self-steepening (SS), and Raman self-scattering (RSS) [21]. These numerical experiments provide a rigorous test bed for comparing the accuracy of the staggered and unstaggered FDTD-ADE schemes. Higher-order solitons are nonlinear superpositions of single solitons with no binding energy. In the presence of small perturbations, they decay and split into their single-soliton constituents. Their decay has been investigated for a variety of cases, including the effects of TOD, SS, and SRS [22, 23]. The dynamics of their decay is very rich due to nonlinear interactions among the multiple single constitutive solitons. Striking examples include the breakup of higher-order soliton pulses under the action of two-photon absorption (TPA) and the complicated evolution of these solitons under periodic amplification. Higher-order solitons have received less attention than fundamental solitons mainly because they are not as robust. However, they exhibit important features like periodic beating [24] due to phase interference among the constitutive solitons, and therefore offer potential applications in switching devices.

2. THE NONLINEAR MAXWELL'S EQUATIONS

Maxwell's equations describing the propagation of light in nonlinear dispersive environments with no free charges are expressed in terms of (**E**, **H**) the electric and magnetic

fields, respectively, and ($\mathbf{D}$, $\mathbf{B}$) the corresponding electric and magnetic flux densities, as

$$\begin{aligned} \nabla \times \mathbf{E} &= -\frac{\partial}{\partial t}\mathbf{B}, \\ \nabla \times \mathbf{H} &= \frac{\partial}{\partial t}\mathbf{D}. \end{aligned} \tag{1}$$

For nonmagnetic media the constitutive relations take the form

$$\begin{aligned} \mathbf{B} &= \mu_0 \mathbf{H}, \\ \mathbf{D} &= \epsilon_0 \mathbf{P}^{\mathrm{TOT}}, \end{aligned} \tag{2}$$

where μ_0, ϵ_0, are the free space permeability and permittivity. The total polarization

$$\mathbf{P}^{\mathrm{TOT}} = \mathbf{P} + \mathbf{P}^{\mathrm{NL}} \tag{3}$$

is related to the electric field through the relations

$$\mathbf{P} = \int_{-\infty}^{t} \chi^{(1)}(t - t_1)\mathbf{E}(t_1)\, dt_1, \tag{4}$$

$$\mathbf{P}^{\mathrm{NL}} = \mathbf{E}(t) \int_{-\infty}^{t} \chi^{(3)}(t - t_1)\|\mathbf{E}(t_1)\|^2\, dt_1. \tag{5}$$

Here, for simplicity, we have assumed [27] (i) axially symmetric and isotropic environments so that the second-order susceptibility tensor $\chi^{(2)}$ is identically zero, (ii) $\chi^{(1)} = \chi^{(1)}_{yy} = \chi^{(1)}_{zz}$, (iii) $\chi^{(3)} = \chi^{(3)}_{yyyy} = \chi^{(3)}_{zzzz}$, and (iv) simplification of the third-order susceptibility into a single nonlinear time convolution involving the field intensity. The susceptibilities can be decomposed into their instantaneous background and residual parts

$$\chi^{(1)}(t) = \epsilon_\infty \delta(t) + \chi^{(1)}_{\mathrm{R}}(t), \tag{6}$$

$$\chi^{(3)}(t) = a(1 - \theta)\delta(t) + \chi^{(3)}_{\mathrm{R}}(t), \tag{7}$$

where ϵ_∞ is the infinite frequency permittivity, $\chi^{(1)}_{\mathrm{R}}$ and $\chi^{(3)}_{\mathrm{R}}$ are the residual susceptibilities, a is the third-order coupling constant, and θ parameterizes the relative strength of the instantaneous electronic Kerr and residual Raman molecular vibrational responses. This decomposition yields

$$\mathbf{P} = \epsilon_\infty \mathbf{E} + \mathbf{\Phi}, \tag{8}$$

$$\mathbf{P}^{\mathrm{NL}} = a(1 - \theta)\|\mathbf{E}\|^2 \mathbf{E} + \mathbf{\Phi}^{\mathrm{NL}}, \tag{9}$$

where $\mathbf{\Phi}$, $\mathbf{\Phi}^{\mathrm{NL}}$ are the residual linear and nonlinear polarizations,

$$\begin{aligned} \mathbf{\Phi}(t) = \int_{-\infty}^{t} \chi^{(1)}_{\mathrm{R}}(t - t_1)\mathbf{E}(t_1)\, dt_1 = \int_{0}^{\infty} \chi^{(1)}_{\mathrm{R}}(t_1)\mathbf{E}(t - t_1)\, dt_1, \\ \mathbf{\Phi}^{\mathrm{NL}}(t) = a\theta \mathcal{Q}\mathbf{E}, \end{aligned} \tag{10}$$

$$\mathcal{Q} = \int_{-\infty}^{t} \chi_{\mathrm{R}}^{(3)}(t-t_1)\|\mathbf{E}(t_1)\|^2\, dt_1. \tag{11}$$

$\mathcal{Q}$ describes the natural molecular vibrations within the dielectric material with frequency many orders of magnitude less than the optical wave frequency, responding to the field intensity. The total third-order nonlinear polarization $\mathbf{P}^{\mathrm{NL}}$ reduces to the instantaneous intensity-dependent Kerr response in the limit $\theta \to 0$.

In terms of the temporal Fourier transform

$$\begin{aligned} E(t) &= \frac{1}{2\pi}\int_{-\infty}^{\infty} \hat{E}(\omega)\exp(i\omega t)\, d\omega, \\ \hat{E}(\omega) &= \int_{-\infty}^{\infty} E(t)\exp(-i\omega t)\, dt, \end{aligned} \tag{12}$$

the residual kernel functions $\chi_{\mathrm{R}}^{(1)}$, $\chi_{\mathrm{R}}^{(3)}$ are modeled by single-resonance Lorentz dipole oscillators (second-order filters):

$$\begin{aligned} \hat{\chi}_{\mathrm{R}}^{(1)}(\omega) &= \frac{\beta_1\omega_1^2}{\omega_1^2 + 2i\gamma\omega - \omega^2}, \\ \hat{\chi}_{\mathrm{R}}^{(3)}(\omega) &= \frac{\Omega_{\mathrm{V}}^2}{\Omega_{\mathrm{V}}^2 + 2i\gamma_{\mathrm{V}}\omega - \omega^2}, \end{aligned} \tag{13}$$

where ω_1, γ, Ω_{V}, γ_{V}, characterize the resonance frequency and bandwidth of the Lorentz dipole oscillators modeling the medium linear and nonlinear residual response, respectively, and β_1 is the difference between the zero (static) and infinite frequency relative permittivity, $\beta_1 = \epsilon_{\mathrm{S}} - \epsilon_{\infty}$, which measures the strength of the field coupling to the linear Lorentz dispersion model. The limit $\beta_1 \to 0$ corresponds to the limiting analytical linear dispersionless case.

In the time domain, the kernel functions obey damped harmonic oscillator ordinary differential equations (ODEs) of motion:

$$\begin{aligned} \ddot{\chi}_{\mathrm{R}}^{(1)}(t) + 2\gamma\dot{\chi}_{\mathrm{R}}^{(1)}(t) + \omega_1^2\chi_{\mathrm{R}}^{(1)} &= 0, \\ \ddot{\chi}_{\mathrm{R}}^{(3)} + 2\gamma_{\mathrm{V}}\dot{\chi}_{\mathrm{R}}^{(3)} + \Omega_{\mathrm{V}}^2\chi_{\mathrm{R}}^{(3)} &= 0. \end{aligned} \tag{14}$$

For the initial conditions $\chi_{\mathrm{R}}^{(1)}(0) = \chi_{\mathrm{R}}^{(3)}(0) = 0$, $\dot{\chi}_{\mathrm{R}}^{(1)}(0) = \omega_{\mathrm{p}}^2$, $\dot{\chi}_{\mathrm{R}}^{(3)}(0) = \Omega_{\mathrm{V}}^2$, the solutions take the form

$$\begin{aligned} \chi_{\mathrm{R}}^{(1)}(t) &= \frac{\omega_{\mathrm{p}}^2}{\nu_0}\exp(-\gamma t)\sin(\nu_0 t)\Theta(t), \\ \chi_{\mathrm{R}}^{(3)}(t) &= \frac{\Omega_{\mathrm{V}}^2}{\nu_{\mathrm{V}}}\exp(-\gamma_{\mathrm{V}} t)\sin(\nu_{\mathrm{V}} t)\Theta(t), \end{aligned} \tag{15}$$

where $\nu_0 = \sqrt{\omega_1^2 - \gamma^2}$, $\omega_{\mathrm{p}}^2 = \beta_1\omega_1^2$ is the plasma frequency, and $\nu_{\mathrm{V}} = \sqrt{\Omega_{\mathrm{V}}^2 - \gamma_{\mathrm{V}}^2}$.

We further simplify Maxwell's equations by considering isotropic and homogeneous media, which permits a one-dimensional formulation of the electromagnetic field propagation problem. For electromagnetic plane waves propagating in the x direction, the vector

Maxwell's equations (1) are expressed as

$$\begin{aligned}
\frac{\partial}{\partial t} H_y &= \frac{1}{\mu_0} \frac{\partial}{\partial x} E_z, \\
\frac{\partial}{\partial t} H_z &= -\frac{1}{\mu_0} \frac{\partial}{\partial x} E_y, \\
\frac{\partial}{\partial t} D_y &= -\frac{\partial}{\partial x} H_z, \\
\frac{\partial}{\partial t} D_z &= \frac{\partial}{\partial x} H_y, \\
\mathbf{D} &= \epsilon_0 \left[\epsilon_\infty \mathbf{E} + a(1-\theta)\, \mathbf{E}\left(E_y^2 + E_z^2\right) + \mathbf{\Phi}^{\mathrm{TOT}} \right],
\end{aligned} \tag{16}$$

where $\mathbf{\Phi}^{\mathrm{TOT}} = \mathbf{\Phi} + \mathbf{\Phi}^{\mathrm{NL}}$ is the total residual polarization. Assuming linearly polarized electromagnetic plane waves, the previous system reduces to

$$\begin{aligned}
\frac{\partial}{\partial t} H &= \frac{1}{\mu_0} \frac{\partial}{\partial x} E, \\
\frac{\partial}{\partial t} D &= \frac{\partial}{\partial x} H, \\
D &= \epsilon_0 [\epsilon_\infty E + a(1-\theta) E^3 + \Phi^{\mathrm{TOT}}],
\end{aligned} \tag{17}$$

where $H = H_y$, $E = E_z$, $D = D_z$, and $\Phi^{\mathrm{TOT}} = \Phi_z + \Phi_z^{\mathrm{NL}}$.

Using Eq. (14), we can treat the memory integrals Φ, $\mathcal{Q}$ as new dependent variables governed by driven damped Lorentz oscillator equations:

$$\ddot{\Phi} + 2\gamma \dot{\Phi} + \omega_1^2 \Phi = \beta_1 \omega_1^2 E, \tag{18}$$

$$\ddot{\mathcal{Q}} + 2\gamma_{\mathrm{V}} \dot{\mathcal{Q}} + \Omega_{\mathrm{V}}^2 \mathcal{Q} = \Omega_{\mathrm{V}}^2 E^2. \tag{19}$$

Following the ADE method, Eqs. (18) and (19) are coupled simultaneously to Maxwell's curl equations (17). However, as shown by Petropoulos [11], these second-order ODEs should be solved as a first-order system in accordance with Maxwell's equations in order to avoid instability due to incorrect time centering in the discrete form of the equations. This can be accomplished by introducing the linear polarization current J and the nonlinear conductivity term σ. The full nonlinear model equations then become

$$\begin{aligned}
\frac{\partial H}{\partial t} &= c\, \frac{\partial E}{\partial x}, \\
\frac{\partial D}{\partial t} &= c\, \frac{\partial H}{\partial x}, \\
\frac{\partial \Phi}{\partial t} &= J, \\
\frac{\partial J}{\partial t} &= -2\gamma J - \omega_1^2 \Phi + \beta_1 \omega_1^2 E, \\
\frac{\partial \mathcal{Q}}{\partial t} &= \sigma, \\
\frac{\partial \sigma}{\partial t} &= -2\gamma_{\mathrm{V}} \sigma - \Omega_{\mathrm{V}}^2 \mathcal{Q} + \Omega_{\mathrm{V}}^2 E^2, \\
D &= \epsilon_\infty E + \Phi + a(1-\theta)\theta E^3 + a\theta \mathcal{Q}\, E.
\end{aligned} \tag{20}$$

The model system (20) results from the dimensional Maxwell equations by scaling all fields and the nonlinear coupling constant on a reference electric field E_0 as

$$\begin{gathered}(H/E_0)\sqrt{\mu_0/\epsilon_0} \to H, \qquad D/(\epsilon_0 E_0) \to D, \qquad \Phi/E_0 \to \Phi, \qquad J/E_0 \to J, \\ E/E_0 \to E, \qquad \mathcal{Q}/E_0^2 \to \mathcal{Q}, \qquad \sigma/E_0^2 \to \sigma \qquad a E_0^2 \to a,\end{gathered} \tag{21}$$

where $\sqrt{\mu_0/\epsilon_0}$ is the free-space impedance. Subsequently scaling time (frequency) on a reference time (inverse time) scale t_0 (t_0^{-1}), and space (wave number) on a reference distance (inverse distance) scale x_0 (x_0^{-1}), results in dimensionless Maxwell's equations. A convenient choice that will be made here for the distance unit corresponds to the free-space distance $x_0 = ct_0$.

Before we describe the numerical schemes in more detail, it is useful to derive the effective linear and nonlinear refractive indices and absorption coefficients. In the time domain, Eqs. (17) are equivalently expressed in the form of a scaled wave equation:

$$\epsilon_\infty \frac{\partial^2}{\partial t^2} E + a(1-\theta)\frac{\partial^2}{\partial t^2} E^3 - \frac{\partial^2}{\partial x^2} E + \frac{\partial^2}{\partial t^2}\Phi^{\mathrm{TOT}} = 0. \tag{22}$$

In Fourier space, the dimensionless electromagnetic fields can be expressed in terms of an envelope and a carrier wave:

$$\begin{bmatrix} E(x,t) \\ H(x,t) \\ D(x,t) \end{bmatrix} = \frac{1}{2}\begin{bmatrix} q(x,t) \\ h(x,t) \\ d(x,t) \end{bmatrix} \exp[i(k_0 x - \omega_0 t)] + c.c. \tag{23}$$

Assuming the rotating wave approximation, that is, neglecting the third-harmonic field, the following wave equation for the slowly varying envelope (SVE) $\hat{q}(x, \omega - \omega_0)$ can be derived,

$$\frac{\partial^2}{\partial x^2}\hat{q}(x, \omega - \omega_0) + \epsilon_{\mathrm{r}}^{\mathrm{TOT}}(\omega)\, \omega^2\, \hat{q}(x, \omega - \omega_0) = 0, \tag{24}$$

where the relative dielectric function is given by

$$\begin{aligned}\epsilon_{\mathrm{r}}^{\mathrm{TOT}}(\omega) &= \epsilon_{\mathrm{r}} + \epsilon_{\mathrm{r}}^{\mathrm{NL}}, \\ \epsilon_{\mathrm{r}} &= \epsilon_\infty + \hat{\chi}_{\mathrm{R}}^{(1)}(\omega), \\ \epsilon_{\mathrm{r}}^{\mathrm{NL}} &= \tfrac{3}{4}\hat{\chi}^{(3)}(\omega - \omega_0)\, a|q|^2,\end{aligned} \tag{25}$$

with $\epsilon_\infty \equiv 1 + \hat{\chi}_\infty^{(1)}$. The single-resonance Lorentz model is characterized by an absorption band lying approximately in the range $[\omega_1, \omega_1\sqrt{\epsilon_{\mathrm{S}}/\epsilon_\infty}]$. The nonlinear dimensionless dispersion relation takes the form

$$\epsilon_{\mathrm{r}}^{\mathrm{TOT}}(\omega)\, \omega^2 = k^2. \tag{26}$$

Its real and imaginary parts are related to the refractive index $n(\omega)$ and the absorption loss

coefficient $\alpha(\omega)$ through the relationship

$$\epsilon_{\mathrm{r}}^{\mathrm{TOT}}(\omega) = \left[n(\omega) + i \frac{\alpha(\omega)}{2\omega} \right]^2. \tag{27}$$

Therefore,

$$\begin{aligned} n(\omega) &= n_0(\omega) + n_2 |q|^2, \\ \alpha(\omega) &= \alpha_0(\omega) + \alpha_2(\omega - \omega_0)|q|^2, \end{aligned} \tag{28}$$

where the linear and nonlinear induced refractive indices are given by

$$\begin{aligned} n_0(\omega) &= \mathcal{R}e\left[\sqrt{\epsilon_\infty + \hat{\chi}_{\mathrm{R}}^{(1)}(\omega)} \right], \\ n_2 &= \frac{3a\hat{\chi}^{(3)}(0)}{8n_0(\omega_0)} = \frac{3a}{8n_0}, \end{aligned} \tag{29}$$

while the single- and two-photon dimensionless absorption coefficients are

$$\begin{aligned} \alpha_0(\omega) &= \frac{\omega_0}{n_0(\omega_0)} \mathcal{I}m\left[\hat{\chi}_{\mathrm{R}}^{(1)}(\omega) \right], \\ \alpha_2(\omega - \omega_0) &= \frac{a\theta\omega_0}{n_0(\omega_0)} \mathcal{I}m\left[\hat{\chi}_{\mathrm{R}}^{(3)}(\omega - \omega_0) \right]. \end{aligned} \tag{30}$$

3. THE NUMERICAL SCHEMES

The Maxwell system (20) is discretized assuming two different spatial configurations: a staggered Yee grid and an unstaggered Liu grid. We consider both second- and fourth-order-accurate approximations to the spatial derivatives on the staggered Yee grids and third-order spatial accuracy on the unstaggered grid. Time integration is performed with the usual second-order leapfrog method where the electric and magnetic fields are staggered in time by an interval $\Delta t/2$. As discussed in the previous section, we solve the second-order auxiliary differential equations as a sequence of first-order differential equations to obtain correct time centering.

3.1. *Yee Staggered Scheme*

In the standard Yee grid, the electric and magnetic fields are staggered in space by half a grid cell. The discretized version of the dimensionless Maxwell curl equations are given by

$$\begin{aligned} \frac{H_{j+1/2}^{n+1/2} - H_{j+1/2}^{n-1/2}}{\Delta t} &= \frac{A\left(E_{j+1}^n - E_j^n\right) + B\left(E_{j+2}^n - E_{j-1}^n\right)}{\Delta x} \\ \frac{D_j^{n+1} - D_j^n}{\Delta t} &= \frac{A\left(H_{j+1/2}^{n+1/2} - H_{j-1/2}^{n+1/2}\right) + B\left(H_{j+3/2}^{n+1/2} - E_{j-3/2}^{n+1/2}\right)}{\Delta x}, \end{aligned} \tag{31}$$

where $(A=1,\ B=0)$ and $(A=9/8,\ B=-1/24)$ correspond respectively to the second- and fourth-order spatially accurate Y22 and Y24 schemes. The discretized version of the dimensionless auxiliary ODEs are given by

$$\begin{aligned}
\frac{\Phi_j^{n+1}-\Phi_j^n}{\Delta t} &= \frac{J_j^{n+1}+J_j^n}{2}\\
\frac{J_j^{n+1}-J_j^n}{\Delta t} &= -2\gamma\frac{J_j^{n+1}+J_j^n}{2}-\omega_1^2\frac{\Phi_j^{n+1}+\Phi^n}{2}+\beta_1\omega_1^2\frac{E_j^{n+1}+E_j^n}{2}\\
\frac{\mathcal{Q}_j^{n+1}-\mathcal{Q}_j^n}{\Delta t} &= \frac{\sigma_j^{n+1}+\sigma_j^n}{2}\\
\frac{\sigma_j^{n+1}-\sigma_j^n}{\Delta t} &= -2\gamma_{\mathrm{V}}\frac{\sigma_j^{n+1}+\sigma_j^n}{2}-\Omega_{\mathrm{V}}^2\frac{\mathcal{Q}_j^{n+1}+\mathcal{Q}_j^n}{2}+\Omega_{\mathrm{V}}^2\frac{\left(E_j^{n+1}+E_j^n\right)^2}{4}\\
D_j^{n+1}-\Phi_j^{n+1} &= E_j^{n+1}\left[\epsilon_\infty+a(1-\theta)\left(E_j^{n+1}\right)^2+a\theta\mathcal{Q}_j^{n+1}\right].
\end{aligned} \tag{32}$$

3.2. *Liu Unstaggered NS2 Scheme*

In the unstaggered grid configuration, all field components of each field vector are colocated. Furthermore, both the electric and magnetic field vectors are defined at the same spatial points. Using FD/BD for the spatial derivatives yields the following discrete PDEs:

$$\begin{aligned}
\frac{H_j^{n+1/2}-H_j^{n-1/2}}{\Delta t} &= -\frac{\left(a_{-1}E_{j+1}^n+a_0E_j^n\right)+\left(a_{-2}E_{j+2}^n+a_1E_{j-1}^n\right)}{\Delta x}\\
\frac{D_j^{n+1}-D_j^n}{\Delta t} &= \frac{\left(a_{-1}H_{j-1}^{n+1/2}+a_0H_j^{n+1/2}\right)+\left(a_{-2}H_{j-2}^{n+1/2}+a_1H_{j+1}^{n+1/2}\right)}{\Delta x}.
\end{aligned} \tag{33}$$

The discrete auxiliary ODEs are the same as in Eq. (32). For the NS2 scheme, $a_{-1}=-1,\ a_0=1/2,\ a_{-2}=1/6, a_1=1/3$ [19].

In the next section, the stability and accuracy of the Y22, Y24, and NS2 schemes are compared for electromagnetic propagation in a *linear* Lorentz dielectric. Therefore, we set $a=0$ in Eq. (20) and omit the nonlinear polarization field.

4. LINEAR STABILITY AND ACCURACY ANALYSIS

Neglecting boundary conditions, the Von Neumann stability analysis [28] assumes a space harmonic variation $e^{ik_{\mathrm{num}}j\Delta x}$ and complex time eigenvalue ξ^n of all the field solutions of the difference equations, i.e., $X_j^n=X^n\,e^{ik_{\mathrm{num}}j\Delta x}$. Inserting this spatially harmonic form into the difference equations yields a linear system of the form $\mathcal{A}\mathbf{X}^{n+1}=\mathcal{B}\mathbf{X}^n$, where $\mathbf{X}$ is the column vector containing all the amplitudes X and $\mathcal{A},\ \mathcal{B}$ are matrices involving $\Delta t, k_{\mathrm{num}}\Delta x$ and the medium parameters. The field growth per time step (time eigenvalues) can then be determined by finding the roots of the characteristic polynomial of $\mathcal{A}^{-1}\mathcal{B}$. If any of these eigenvalues are outside the unit circle for any $k_{\mathrm{num}}\Delta x$ in the range $0\le k_{\mathrm{num}}\Delta x\le\pi$, then the scheme is unstable.

The resulting characteristic polynomial is

$$\xi^4\left[\epsilon_\infty(1+\gamma\Delta t)+\frac{\omega_1^2\Delta t^2}{4}\epsilon_S\right]+\xi^3\left[\eta\left(1+\gamma\Delta t+\frac{\omega_1^2\Delta t^2}{4}\right)-2\epsilon_\infty(2+\gamma\Delta t)\right]$$
$$+\xi^2\left[\eta\left(-2+\frac{\omega_1^2\Delta t^2}{2}\right)+6\epsilon_\infty-\frac{\omega_1^2\Delta t^2}{2}\epsilon_S\right]+\xi\left[\eta\left(1-\gamma\Delta t+\frac{\omega_1^2\Delta t^2}{4}\right)\right.$$
$$\left.-2\epsilon_\infty(2-\gamma\Delta t)\right]+\left[\epsilon_\infty(1-\gamma\Delta t)+\frac{\omega_1^2\Delta t^2}{4}\epsilon_S\right]=0, \tag{34}$$

where for the staggered Yee and unstaggered Liu schemes respectively

$$\begin{aligned}\eta_{Y22}&=4\nu_{Y22}^2\sin^2(k_{num}\Delta x/2),\\ \eta_{Y24}&=4\nu_{Y24}^2\left[\tfrac{9}{8}\sin(k_{num}\Delta x/2)-\tfrac{1}{24}\sin(3k_{num}\Delta x/2)\right]^2,\\ \eta_{NS2}&=\nu_{NS2}^2\left[\tfrac{25}{18}+\tfrac{1}{9}\cos(3k_{num}\Delta x)-\tfrac{1}{2}\cos(2k_{num}\Delta x)-\cos(k_{num}\Delta x)\right],\end{aligned} \tag{35}$$

and $\nu=\Delta t/\Delta x$ are the CFL numbers. The characteristic polynomial (34) is fourth-order in ξ because the second-order Lorentz ODE for the polarization was transformed to a first-order system in accordance with Maxwell's equations. Its four complex roots may be easily obtained using a straightforward short Mathematica code. Since even and odd powers of ξ are present in Eq. (34), the even–odd field coupling is preserved by all schemes. The maximum CFL number for which $|\xi|\le 1$ can be calculated analytically by solving the inequalities $\eta\le 4\epsilon_\infty$, yielding

$$\begin{aligned}\nu_{Y22}&\le\sqrt{\epsilon_\infty},\\ \nu_{Y24}&\le\frac{6\sqrt{\epsilon_\infty}}{7},\\ \nu_{NS2}&\le\frac{4\sqrt{\epsilon_\infty}}{3}.\end{aligned} \tag{36}$$

Interestingly, all schemes have a stability criterion that depends only on ϵ_∞ and is independent of all other medium parameters. Also, we note that the NS2 scheme has the largest maximum stable CFL number. The maximum value of ν_{Y22} corresponds to the magic time step zeroing numerical dispersion when modeling dispersionless media.

The amount of artificial dissipation introduced by the discrete ODEs is shown in Fig. 1 as a function of the grid resolution $k_{num}\Delta x$ for a fixed normalized CFL number ν/ν_{max} equal to 1 and 0.7 (this last value lying slightly below the maximum CFL number $1/\sqrt{2}$ for the Y22 scheme in 2D [1]). We consider the parameter values $\epsilon_S=5.25$, $\epsilon_\infty=2.25$ as in [3] and a medium resonance-frequency resolution $\omega_1\Delta t=2\pi/60\sim 10^{-1}$. The case of a low-loss Lorentz medium with $\gamma/\omega_1=0.01$ is shown. The discretization-induced numerical dissipation is very small for all schemes, with a peak value of $\sim 5\times 10^{-4}$. We note that NS2 has a slightly narrower peak in both graphs.

Assuming a space-time harmonic variation $e^{i(\omega t-kx)}$ of all fields, the exact (physical) dispersion relation associated with the linear part of Eq. (20) is readily obtained in dimensionless form as

$$\epsilon_\infty\omega^4+2i\epsilon_\infty\gamma\omega^3-\left[k^2+\epsilon_S\omega_1^2\right]\omega^2-2i\gamma k^2\omega+k^2\omega_1^2=0. \tag{37}$$

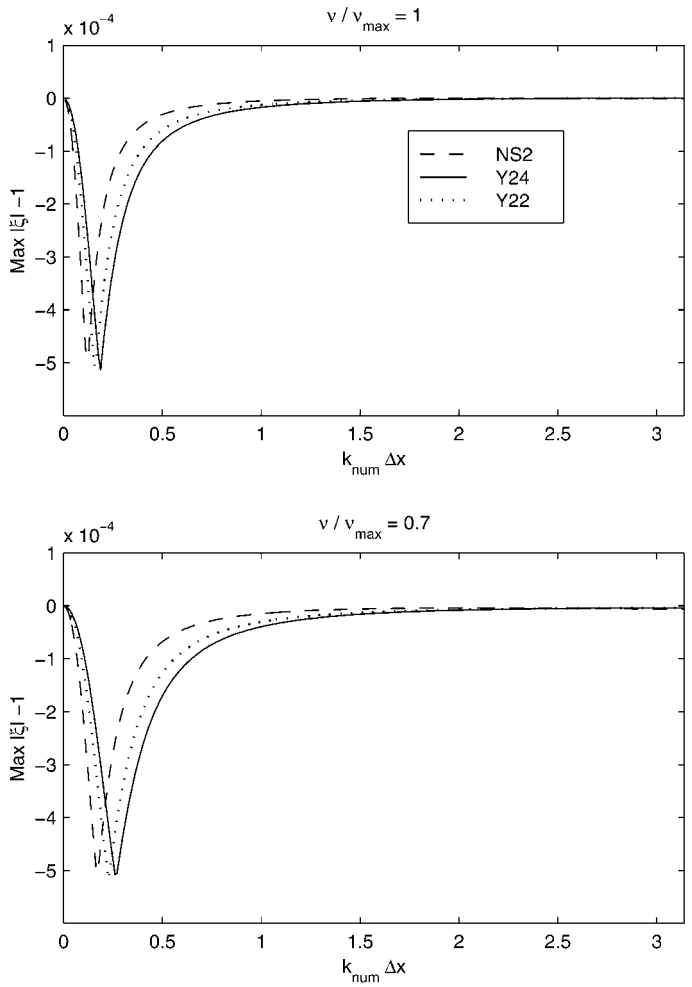

FIG. 1. Largest magnitude of the four complex roots of the characteristic polynomial (Eq. (34)) as a function of grid resolution $k_{\text{num}}\Delta x$ for a low-loss Lorentz medium with $\gamma/\omega_1 = 0.01$, $\epsilon_S = 5.25$, $\epsilon_\infty = 2.25$, and $\omega_1 \Delta t = 2\pi/60 \sim 10^{-1}$. The normalized CFL number $v/v_{\max}$ is equal to 1 (top) and 0.7 (bottom).

For an arbitrary choice of characteristic space length x_0, the dispersion relation has the same form if we substitute $k \to k(ct_0/x_0)$ in Eq. (37). The solution of this physical dispersion relation is readily obtained as

$$k = \omega \sqrt{\epsilon_\infty} \sqrt{1 - \frac{(\beta_1/\epsilon_\infty)\omega_1^2}{\omega^2 + 2i\gamma\omega - \omega_1^2}}. \tag{38}$$

Plots of the exact refractive index and attenuation constant are shown in Fig. 2 for a low-loss Lorentz medium with $\gamma/\omega_1 = 0.01$, $\epsilon_S = 5.25$, and $\epsilon_\infty = 2.25$. The abrupt change in the refractive index at $\omega/\omega_1 = 1$ and $\omega/\omega_1 = \sqrt{\epsilon_S/\epsilon_\infty} \sim 1.527$ defines the edges of the Lorentz absorption band.

The numerical dispersion relation satisfied by the finite-difference approximations of the linear model equations (neglecting boundary conditions) are found in the same way by assuming an $e^{i(\omega n \Delta t - k_{\text{num}} j \Delta x)}$ variation for the field quantities, with n and j enumerating the

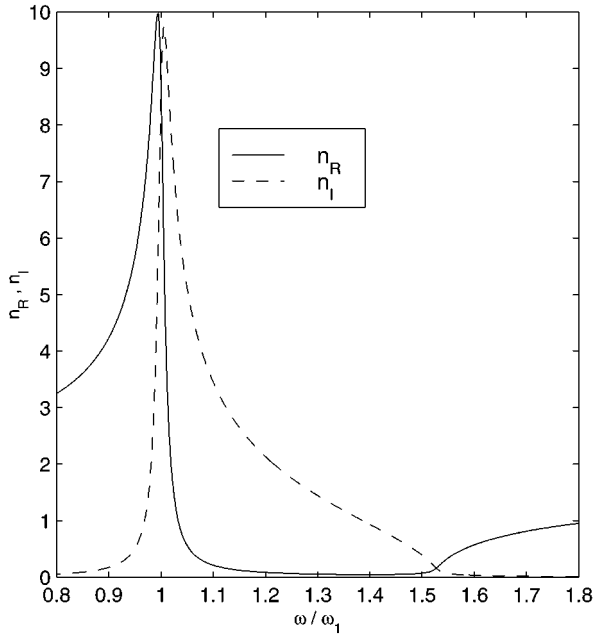

FIG. 2. Exact linear refractive index and attenuation coefficient of a Lorentz medium characterized by $\gamma/\omega_1 = 0.01$, $\epsilon_S = 5.25$, and $\epsilon_\infty = 2.25$.

time step and spatial grid point, respectively, yielding

$$\epsilon_\infty \bar{\omega}^4 + i\epsilon_\infty \bar{\gamma}\bar{\omega}^3 - \left[\left(\frac{\eta}{4\Delta t^2}\right) + \epsilon_S \frac{\bar{\omega}_1^2}{4}\right]\bar{\omega}^2 - i\bar{\gamma}\bar{\omega}\left(\frac{\eta}{4\Delta t^2}\right) + \left(\frac{\eta}{4\Delta t^2}\right)\frac{\bar{\omega}_1^2}{4} = 0, \quad (39)$$

where η is given by Eq. (35), $\bar{\omega} = \sin(\omega\Delta t/2)/\Delta t$, and the numerical medium relaxation and resonance frequencies are given by

$$\bar{\gamma} = \gamma \cos(\omega\Delta t/2), \quad (40)$$

$$\bar{\omega}_1 = \omega_1 \cos(\omega\Delta t/2). \quad (41)$$

The numerical dispersion relation (39) can be rewritten in the form

$$\frac{\sqrt{\eta}}{2\Delta t} = \bar{\omega}\sqrt{\epsilon_\infty}\sqrt{1 - \frac{(\beta_1/\epsilon_\infty)\bar{\omega}_1^2/4}{\bar{\omega}^2 + i\bar{\gamma}\bar{\omega} - \bar{\omega}_1^2/4}}, \quad (42)$$

where $\sqrt{\eta_{Y24}}$ and η_{NS2} are cubic complex polynomials in $k_{num}\Delta x$ whose analytical solutions are known [16].

The numerical solution may then be compared with the exact physical one given by Eq. (38) as a function of the frequency resolution $\omega\Delta t$ for fixed normalized CFL number $\nu/\nu_{max} \leq 1$, γ/ω_1 and $\omega_1\Delta t$. Figure 3 shows plots of the following quantities: normalized ratio between the numerical and the exact phase velocity (also given by the normalized ratio between the exact and the numerical refractive index); normalized attenuation constant; normalized energy velocity; and normalized group velocity. Parameter values are $\gamma/\omega_1 = 0.01$, $\omega_1\Delta t = 2\pi/60$, $\epsilon_S = 5.25$, and $\epsilon_\infty = 2.25$. The normalized CFL number is set 30% below its

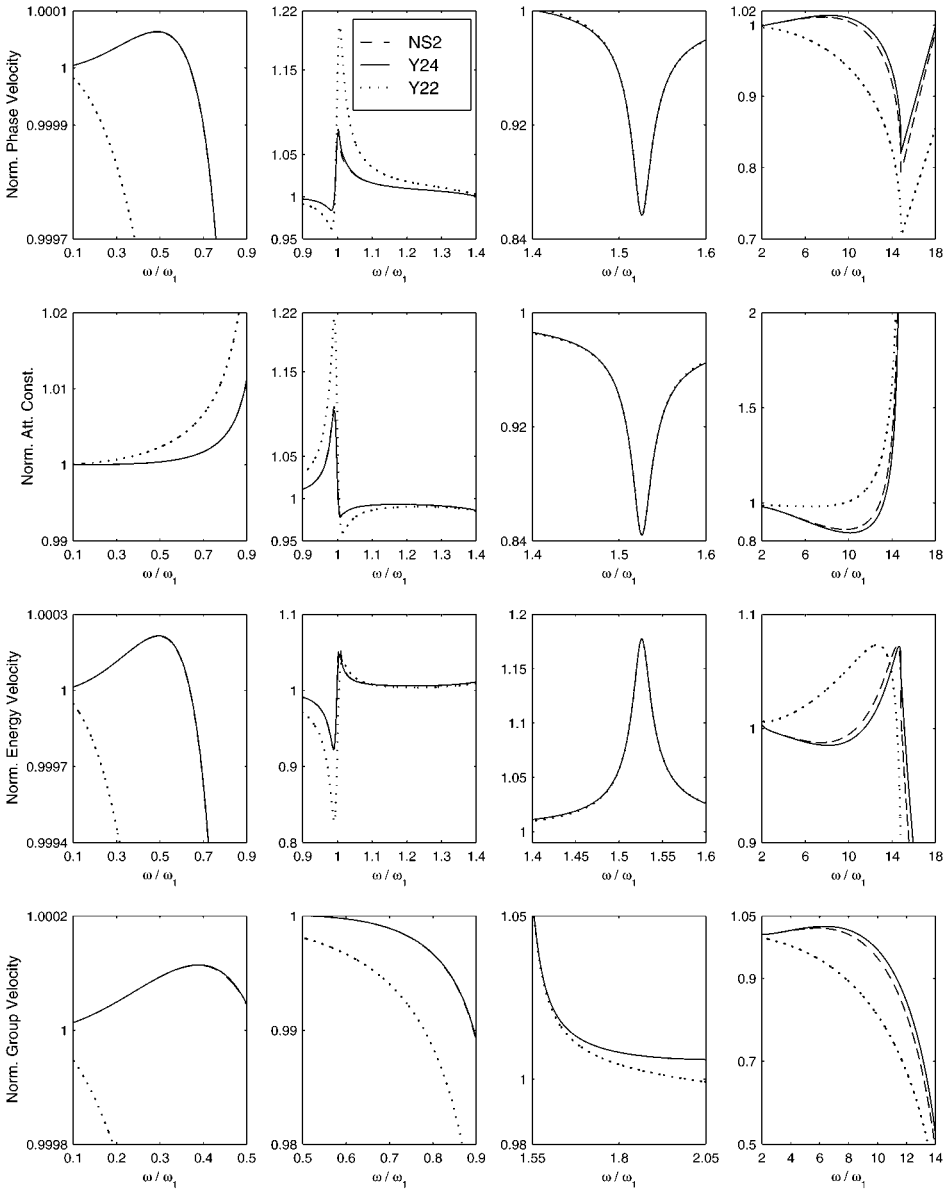

FIG. 3. Normalized phase velocity, attenuation constant, energy velocity, and group velocity across the passband and absorption band of the Lorentz medium ($\gamma/\omega_1 = 0.01$, $\omega_1 \Delta t = 2\pi/60$, $\epsilon_S = 5.25$, $\epsilon_\infty = 2.25$). The normalized CFL number is equal to $\nu/\nu_{\max} = 0.7$.

maximum stability limit, i.e., $\nu/\nu_{\max} = 0.7$. In Fig. 3, the data for each normalized quantity have been graphed across four windows to provide the necessary graphical dynamic range in each frequency regime. The windows illustrate frequency regimes below resonance, near resonance, at the upper edge of the medium absorption band, and far above resonance where the frequencies are coarsely resolved. Figure 3 illustrates the following salient features: (1) All schemes have their highest normalized phase/dissipation errors at the coarsely resolved high frequency (approximately given by $\omega_c/\omega_1 \sim 2/(\omega_1 \Delta t) \sin^{-1}(\nu/\nu_{\max}) \sim 14.8$) beyond which the fields decay exponentially and have an increasing phase velocity [25].

(2) All schemes have the same error level at the upper edge of the medium absorption band (at $\omega/\omega_1 = \sqrt{\epsilon_S/\epsilon_\infty} \sim 1.527$). (3) In comparison to the Y22 scheme, the Y24 and NS2 schemes have reduced phase/dissipation errors at frequencies near the linear resonant frequency ($\omega/\omega_1 \sim 1$) and below ($\omega/\omega_1 < 1$). The energy transport velocity has been calculated according to the formula given in [26],

$$v_E/c = \left[n + \frac{(\epsilon_R - \epsilon_S)(\epsilon_R - \epsilon_\infty) + \epsilon_I^2}{n(\epsilon_S - \epsilon_\infty)} \right]^{-1}, \tag{43}$$

where ϵ_R, ϵ_I are the real and imaginary parts of the relative complex dielectric function. Since the energy velocity decreases in lossy frequency regions, the normalized ratio between the numerical and exact energy velocities goes to zero for frequencies higher than ω_c and has upward peaks when the numerical extinction coefficient is lower than the exact one (i.e., at the upper edge of the medium absorption band). Finally, the group velocity, calculated numerically from the exact and numerical dispersion relations, is shown to behave like the normalized phase velocity in the passbands of the Lorentz model.

Further investigations of the Y22 schemes confirm that it exhibits the lowest phase error at the maximum normalized CFL number, as expected. Further investigations of the Y24 and NS2 schemes reveal that decreasing the normalized CFL number from its maximum value of unity results in a shift in the frequency range over which the maximum error occurs. For normalized CFL numbers near unity, the maximum error occurs at the coarsely resolved high frequencies at the upper end of the Lorentz spectrum. As the CFL number is decreased, the frequency at which the maximum phase error occurs downshifts toward the upper edge of the medium absorption band ($\omega/\omega_1 = \sqrt{\epsilon_S/\epsilon_\infty}$). This trend is illustrated in Fig. 3, where for $\nu/\nu_{max} = 0.7$, the phase error at the upper edge of the absorption band ($\omega/\omega_1 \simeq 1.527$) is nearly at the level of the error seen at the higher coarsely resolved frequencies. As the CFL number is further decreased, the phase error becomes dominant at the medium resonant frequency ($\omega/\omega_1 = 1$).

Finally, we show in Fig. 4 that the NS3 scheme is shown to be unable to capture the correct physics in the medium absorption band. The two complex numerical solutions u_1, u_2 lying closest to the exact one are plotted near the medium resonant frequency, using the same medium parameters as above. ($k_{num}\Delta x$ is obtained by taking the complex arc cosine of those solutions.) Results show that for fixed medium parameters, there is a critical normalized CFL number below which the real parts of u_1, u_2 coalesce, whereas their imaginary parts present both up to two common discontinuities which move toward the upper edge of the absorption band as ν/ν_{max} is further reduced. For this reason, and since this scheme is only first-order [20], we have not included it in any of the other analyses or comparisons in this paper.

In the next section, numerical experiments illustrate the use of the two grid arrangements to study the transient evolution of few-cycle optical localized pulses in a Lorentz dispersive unidimensional environment with *nonlinear* third-order delayed response modeling Raman scattering.

5. NUMERICAL EXPERIMENTS ON TEMPORAL SOLITONS

In this section, numerical simulations of the discrete nonlinear full model equations (31)–(32), (33)–(32) are performed. We use the following normalized electric field source

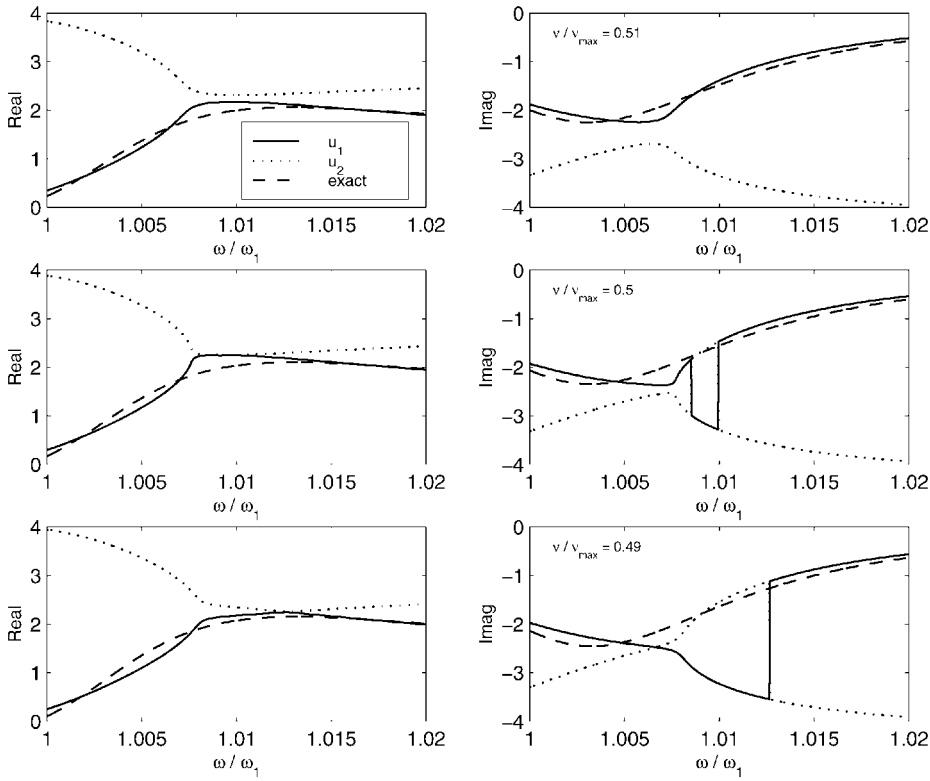

FIG. 4. The two complex numerical solutions u_1, u_2 of the NS3 scheme lying closest to the exact one. Parameter values are $\gamma/\omega_1 = 0.01$, $\omega_1 \Delta t = 2\pi/60$, $\epsilon_S = 5.25$, and $\epsilon_\infty = 2.25$.

condition at the left grid boundary,

$$E(x = 0, t) = f(t) \cos(\omega_0 t), \tag{44}$$

where $f(t) = N \operatorname{sech}(t/t_0)$, t_0 (related to the full width at half-peak intensity by $t_{\mathrm{FWHM}} \simeq 1.76 t_0$) is the characteristic time scale of the initial pulse envelope of normalized peak amplitude N, and N defines the number of solitons forming the multisoliton pulse [24]. The unstaggered grid arrangement requires the additional knowledge of the initial H values, which can be approximately obtained taking into account the linear group velocity (GV) and group velocity dispersion (GVD) of the pulse from the Fourier integral

$$H(x = 0, t) = \int_{-\infty}^{\infty} \hat{H}(\omega) e^{i\omega t} d\omega, \tag{45}$$

where

$$\hat{H}(\omega) = \frac{1}{Z} \hat{E}(\omega), \tag{46}$$

and the linear impedance defined as the ratio of the electric over magnetic Fourier magnitudes is equal to $Z = -\omega/k$. Performing a Taylor expansion of $k(\omega)$ around $\omega = \omega_0$

yields

$$H(x=0,t) \simeq \frac{1}{2}\left[\frac{1}{Z_0} f(t) - i\left(\frac{1}{Z_0}\right)' f'(t) - \frac{1}{2}\left(\frac{1}{Z_0}\right)'' f''(t)\right] e^{i\omega_0 t} + c.c., \quad (47)$$

where the impedance and its derivatives are all calculated at $\omega = \omega_0$.

In order to obtain solitonlike behavior from the balance of dispersion (GVD) and Kerr nonlinearity (SPM), the initial normalized peak amplitude N and pulse width t_0 of the scaled electric field in Eq. (44) have to be properly adjusted according to the nonlinear Schrödinger (NLS) equation. When the electromagnetic fields are assumed to be circularly polarized, a standard reductive perturbation method (RPM) [29] within the slowly varying envelope approximation (SVEA) is used to reduce them to the NLS equation. This asymptotic reduction is carried out in a coordinate system moving with the pulse in space (spatial soliton) or in time (temporal soliton). Formally, this is done by introducing the slowly varying variables $\xi = \epsilon(x - \omega_0' t)$, $\tau = \epsilon^2 t$, or equivalently the dual slow variables $\xi = \epsilon^2 x$, $\tau = \epsilon(t - k_0' x)$ which yields the one-dimensional NLS equation respectively in the form

$$i q_\tau + \frac{1}{2}\frac{\xi_0^2}{T_D} q_{\xi\xi} + \frac{1}{T_{NL}}|q|^2 q = 0, \quad (48)$$

$$i q_\xi + \frac{1}{2}\frac{\tau_0^2}{L_D} q_{\tau\tau} + \frac{1}{L_{NL}}|q|^2 q = 0. \quad (49)$$

ϵ is the small perturbation parameter $\epsilon \sim \mathcal{O}(\Delta\omega/\omega_0) \ll 1$ (quasi-monochromatic approximation).

The characteristic dispersive and nonlinear length scales [21] are given by

$$T_D = \frac{\xi_0^2}{\omega_0''}, \qquad T_{NL} = \frac{2k_0 c^2}{a_{circ}\,\omega_0^2 \omega_0'} = \frac{c}{n_2 \omega_0 \omega_0'}, \quad (50)$$

$$L_D = -\frac{\tau_0^2}{k_0''} = (\omega_0'\tau_0/\xi_0)^2 \omega_0' T_D, \qquad L_{NL} = \omega_0' T_{NL}, \quad (51)$$

where we used the fact that for circular polarization, Eq. (29) is replaced by $a_{circ} \simeq 2n_0 n_2$, that is, $a = (4/3)a_{circ}$. The balance between the dispersive and nonlinear length (time) scales, written respectively as

$$T_{NL} = T_D, \qquad L_{NL} = L_D, \quad (52)$$

provides the appropriate value for the nonlinear parameter a to obtain solitonlike behavior. Note that from the definition of the dual moving frames, $\xi_0 = -\omega_0'\tau_0$, this value is identical in both moving coordinate systems. However, for the Maxwell's equations we have chosen to normalize space by the free-space velocity c, i.e., $\xi_0 = x_0 = ct_0$, and hence $(\omega_0' t_0/x_0)^2 \neq 1$, meaning that the value of a obtained for the driving boundary conditions (Eqs. (44) and (47)) that is used here will be different by a factor $(\omega_0'/c)^2$ from that obtained using initial conditions given by specifying all fields (including the polarization) at $t = 0$ like is done in [17].

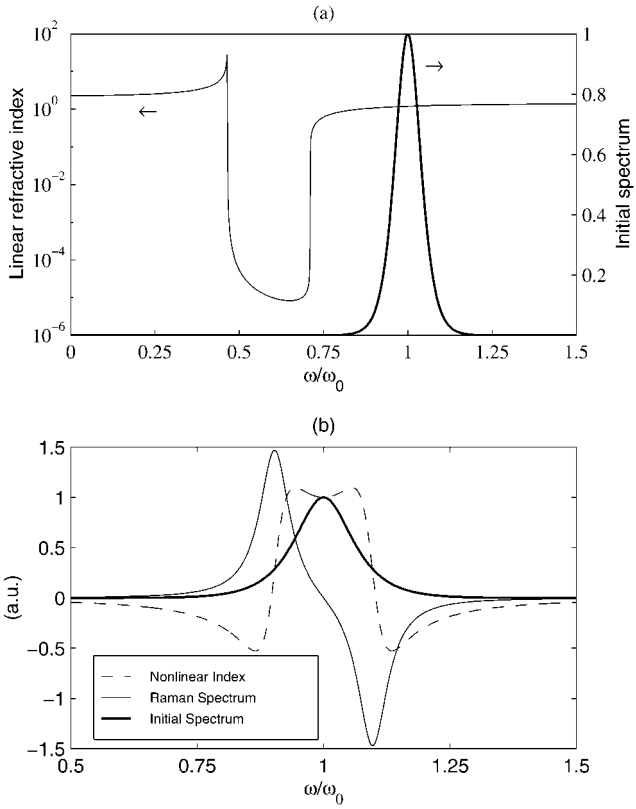

FIG. 5. (a) Linear refractive index and (b) the nonlinear Raman gain and nonlinear index (dashed curve) spectra. The pulse spectrum has been superimposed for comparison. Normalized linear Lorentz and Raman parameters are $\gamma/\omega_1 = 10^{-6}$, $\omega_1 = 5.84$, $\epsilon_S = 5.25$, $\epsilon_\infty = 2.25$, $\theta = 0.3$, $\gamma_V/\Omega_V \simeq 0.356$, and $\Omega_V = 1.28$.

5.1. *Decay of Higher-Order Temporal Solitons*

The physical linear refractive index and the nonlinear Raman gain and nonlinear index (dashed curve) spectra are shown in Fig. 5.

The source spectrum has been superimposed for comparison. The long relaxation time (small damping $\gamma/\omega_1 = 10^{-6}$) of the resonance causes two deep jumps of the linear refractive index at $\omega \sim \omega_1$ and $\omega \sim \omega_1\sqrt{\epsilon_S/\epsilon_\infty}$, which outside this absorption band increases slowly with frequency toward its infinite frequency value of $\sqrt{\epsilon_\infty}$. The Lorentz medium exhibits anomalous (normal) dispersion $\omega'' > 0$ ($\omega'' < 0$) over the spectral domain above (below) the absorption band. We have chosen the same pulse parameters as in [3], i.e., an initial hyperbolic secant bright soliton pulse of duration equal to 25.7 fs (FWHM) (time constant $t_0 = 14.6$ fs, $ct_0 = 4.38$ μm) centered at $\omega_0/2\pi = 137$ THz ($\omega_0 t_0 = 12.57$) (vacuum wavelength $\lambda_0 = 2.19$ μm). Approximately 3.5 modulation cycles are contained within the FWHM. The parameters defining the Raman Lorentz model are [30] $\nu_V^{-1} = 12.2$ fs, $\gamma_V^{-1} = 32$ fs ($\nu_V t_0 \sim 1.2$, $\gamma_V t_0 \sim 0.456$) ($\Omega_V t_0 = 1.28$). The largest gain occurs at a frequency shifted upward by about $\Omega_V t_0$ corresponding to 13.2 THz, which is of the order of the initial soliton spectral width ($\Omega_V/\omega_0 \simeq 0.1$).

Figures 6 and 7 display results of the simulations of transient fundamental ($N = 1$) and second-order ($N = 2$) temporal soliton evolution, propagating in the nonlinear Raman environment.

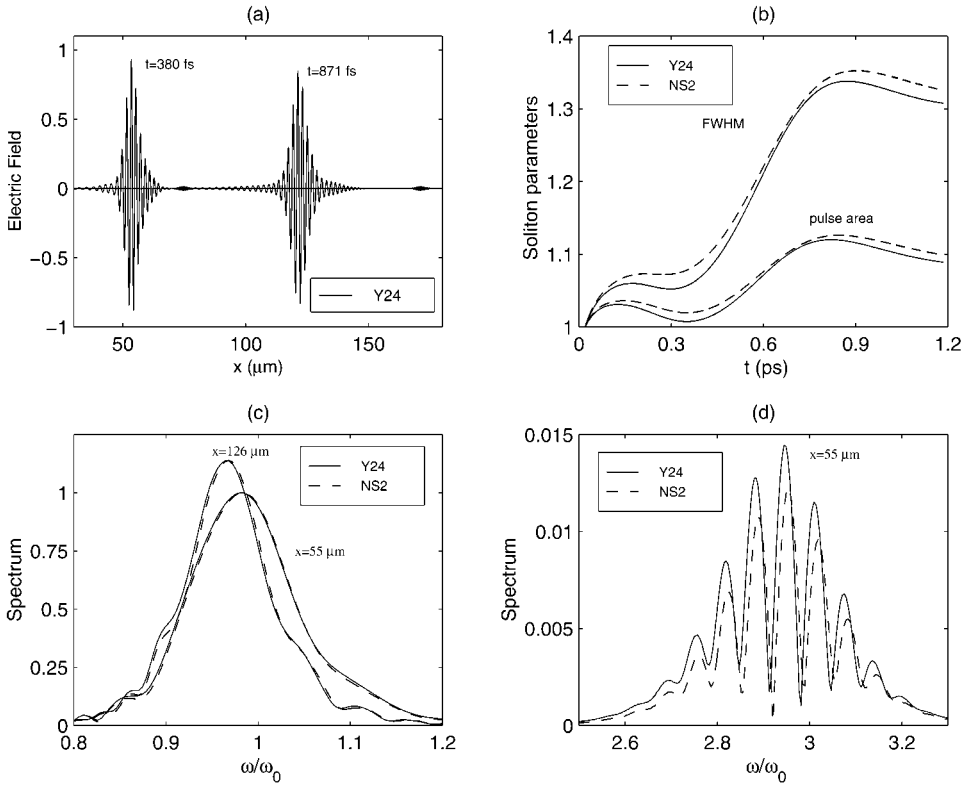

FIG. 6. Transient fundamental ($N = 1$) temporal soliton propagation in the nonlinear Raman environment for the same medium parameters as in Fig. 5.

The relative strength of the Kerr and Raman interactions is chosen equal to $\theta = 0.3$. A simple exact 1D one-way ABC was used. Alternative implementations of radiation boundary conditions for high-order stencils using ghost nodes have been derived by Petropoulos [31] and others. In order to globally preserve the accuracy of the schemes, these were closed near the boundary using fifth- and fourth-order-accurate one-sided approximations as in [32, 33]. All codes were run at half their linear CFL stability limit on a Sun Ultra 10 class workstation with run times below 30 min. in all cases tested using dynamic arrays to minimize storage. All schemes are explicit and need only to call a standard Newton solver for the cubic equation in E^{n+1}.

The pulse central frequency was chosen at $\omega_0/\omega_1 \sim 2.15$ above the absorption band (anomalous dispersion region). The approximate value of a required by the Maxwell's solver to obtain solitonlike dynamics can be obtained from the NLS balance equation (52) for the circular polarization with the choice of distance unit $\xi_0 = x_0 = ct_0$. For the driving boundary condition Eqs. (44) and (47) and taking into account the Raman contribution, this yields $a_{\text{circ}}(1 - \theta) = 3.78 \times 10^{-2}$. For the linear polarization, $a = (4/3)a_{\text{circ}}$, which gives for $\theta = 0.3$ the value $a = 7 \times 10^{-2}$ found by Goorjian and Taflove. Attention must also be paid to ensure sufficient spatial resolution due to the generation of third harmonics.

Several grid sizes have been used to explore the numerical stability and accuracy of the nonlinear codes. A spatial resolution $\Delta x \sim \lambda_0/64$ (λ_0 being the carrier wavelength inside the medium) is sufficient to mitigate the effects of numerical dispersion in the cases

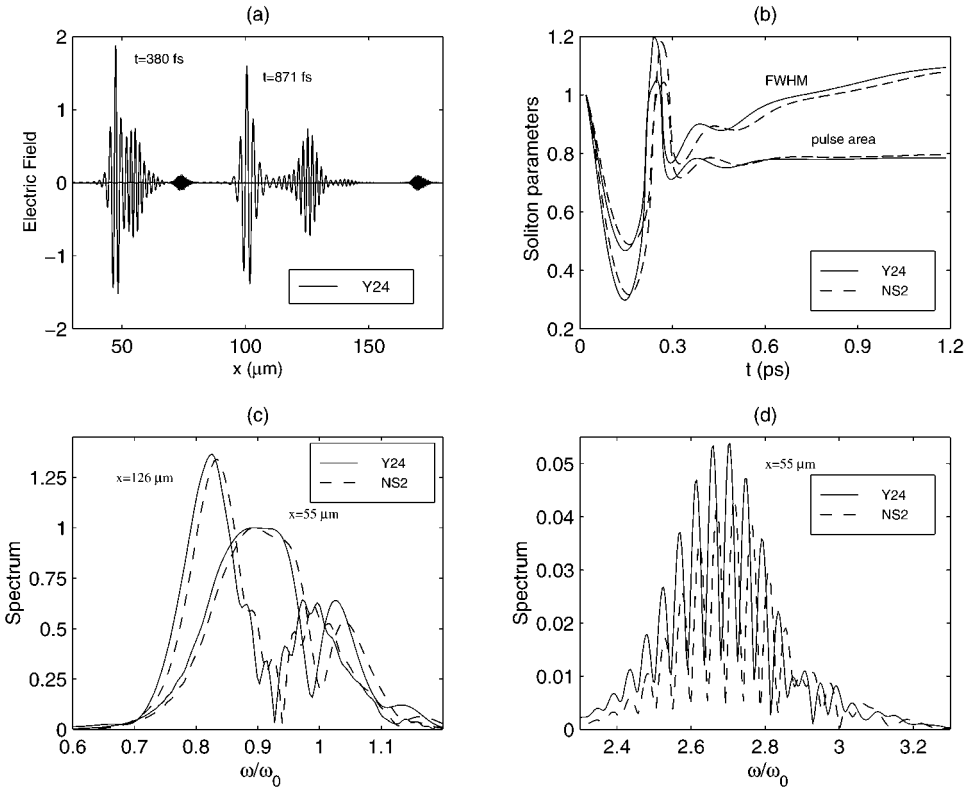

FIG. 7. Transient second-order ($N = 2$) temporal soliton propagation in the nonlinear Raman environment for the same medium parameters as in Fig. 5.

treated. To characterize the solitonlike propagation regime, a useful parameter is given by the product of the peak pulse intensity and the square of its FWHM. For fundamental solitons, this measure of the "pulse area" is constant. Numerical results present excellent agreement between the unstaggered and staggered nonlinear FDTD-ADE schemes. The small (less than 1%) deviation in the soliton parameters (width and pulse area) obtained with the unstaggered grid scheme can be attributed to the approximate source condition needed for the magnetic field colocated with the electric field at $x = 0$. Figures 6a and 7a display the pulse E field at $t = 380$ fs and $t = 871$ fs corresponding to a propagation distance equal to $x = 55\,\mu$m and $x = 126\,\mu$m, respectively. Also shown in Figs. 6b and 7b is the transient evolution of the pulse parameters. Figures 6c and 7c and 6d and 7d depict the pulse fundamental and third-harmonic spectra. The asymptotic height of each soliton resulting from the splitting of the initial second-order soliton (Fig. 7) into its components is roughly $2\lambda_I/N = 3/2, 1/2$, where λ_I are the imaginary eigenvalues obtained from the inverse scattering theory (IST) [24]. Phase velocity mismatch leads to the separation of the transient third-harmonic precursor generated by the initial condition from the main pulse traveling at a different group velocity. As a result of the interference between this transient precursor and the stationary third-harmonic pulse continuously generated and traveling with the main pulse, the third-harmonic spectrum exhibits a symmetric modulation and a continuous redshift due to the Raman self-scattering of the main pulse.

6. CONCLUDING REMARKS

We have developed 1D vector Maxwell's equations solvers based on the staggered grid originally proposed by Yee and an unstaggered NS2 scheme proposed by Liu and shown by Driscoll and Fornberg to be third-order-accurate to study the propagation of temporal solitons in a single-resonance Lorentz medium with third-order Raman-like nonlinearity. The stability and accuracy of the linear version of the various FDTD-ADE schemes have been analyzed. We have found that all schemes have a stability criterion that depends only on ϵ_∞, and that the stability limit for the NS2 scheme is higher than that for the Y22 and Y24 schemes. In comparison to the Y22 schemes, the numerical phase velocity errors for the higher-order schemes are greatly reduced at frequencies below the Lorentz absorption band and around the medium resonance frequency. The numerical dissipation levels do not vary much between schemes, and overall are very small.

We have tested the staggered and unstaggered FDTD-ADE schemes on a relatively complicated class of third-order nonlinear optical problems: the modeling of higher-order solitonlike and third-harmonic dynamics. Numerical results using the unstaggered grid scheme are in excellent agreement with the results obtained using the staggered grid schemes. Use of colocated electric field schemes such as the NS2 unstaggered scheme investigated here may prove to be essential for modeling nonlinear optical pulse propagation in higher dimensions. For this application, the advantage of using an unstaggered grid over an uncolocated staggered grid appears to outweigh any disadvantage of having to use an approximate boundary condition for the unstaggered grid where the fields are colocated.

ACKNOWLEDGMENTS

The authors thank Dr. P. G. Petropoulos and the referees for helpful suggestions. L. Gilles acknowledges the Honorary Fellow appointment at the University of Wisconsin. This work was sponsored in part by the Madrid Autonome Community (CAM) (Spain) and the Comisión Interministerial de Ciencia y Technología of Spain (PB95-0426).

REFERENCES

1. A. Taflove and S. C. Hagness, *Computational Electrodynamics: The Finite-Difference Time-Domain Method*, 2nd ed. (Artech House, Norwood, 2000); K. S. Kunz and R. J. Luebbers, *The Finite Difference Time Domain Method for Electromagnetics* (CRC Press, Boca Raton, 1993).
2. R. M. Joseph, S. C. Hagness, and A. Taflove, Direct time integration of Maxwell's equations in linear dispersive media with absorption for scattering and propagation of femtosecond electromagnetic pulses, *Opt. Lett.* **16**, 1412 (1991).
3. P. M. Goorjian, A. Taflove, R. M. Joseph, and S. C. Hagness, Computational modeling of femtosecond optical solitons from Maxwell's equations, *IEEE J. Quantum Electron.* **28**, 2416 (1992).
4. R. W. Ziolkowski and J. B. Judkins, Full-wave vector Maxwell's equation modeling of the self-focusing of ultrashort optical pulses in a nonlinear Kerr medium exhibiting a finite response time, *J. Opt. Soc. Am. B* **10**, 186 (1993).
5. R. M. Joseph, P. M. Goorjian, and A. Taflove, Direct time integration of Maxwell's equations in 2-D dielectric waveguides for propagation and scattering of femtosecond electromagnetic solitons, *Opt. Lett.* **18**, 491 (1993).
6. R. M. Joseph and A. Taflove, Spatial soliton deflection mechanism indicated by FDTD Maxwell's equations modeling, *IEEE Photon. Technol. Lett.* **6**, 1251 (1994).

7. R. W. Ziolkowski and J. B. Judkins, Applications of the nonlinear finite difference time domain (NL-FDTD) method to pulse propagation in nonlinear media: Self-focusing and linear/nonlinear interfaces, *Radio Sci.* **28**, 901 (1993).
8. R. W. Ziolkowski and J. B. Judkins, Nonlinear finite-difference time-domain modeling of linear and nonlinear corrugated waveguides, *J. Opt. Soc. Am. B* **11**, 1565 (1994).
9. S. A. Basinger and D. J. Brady, Finite-difference time-domain modeling of dispersive nonlinear Fabry–Perot cavities, *J. Opt. Soc. Am. B* **11**, 1504 (1994).
10. R. M. Joseph and A. Taflove, FDTD Maxwell's equations models for nonlinear electrodynamics and optics, *IEEE Trans. Antennas Propag.* **45**, 364 (1997).
11. P. G. Petropoulos, Stability and phase error analysis of FD-TD in dispersive dielectrics, *IEEE Trans. Antennas Propag.* **42**, 62 (1994).
12. J. L. Young, A. Kittichartphayak, Y. M. Kwok, and D. Sullivan, On the dispersion errors related to *(FD)*^{2}*TD* type schemes, *IEEE Trans. Microwave Theory Technol.* **43**, 1902 (1995).
13. S. A. Cummer, An analysis of new and existing FDTD methods for isotropic cold plasma and a method for improving their accuracy, *IEEE Trans. Antennas Propag.* **45**, 392 (1997).
14. K. S. Yee, Numerical solution of initial boundary value problems involving Maxwell's equations in isotropic media, *IEEE Trans. Antennas Propag.* **14**, 302 (1966).
15. P. G. Petropoulos, Phase error control for FD-TD methods of second and fourth order accuracy, *IEEE Trans. Antennas Propag.* **42**, 859 (1994).
16. W. H. Press, *Numerical Recipes in Fortran: The Art of Scientific Computing*, 2nd ed. (Cambridge, Univ. Press, England, 1992).
17. C. V. Hile and W. L. Kath, Numerical solutions of Maxwell's equations for nonlinear-optical pulse propagation, *J. Opt. Soc. Am. B* **13**, 1135 (1996).
18. B. Fidel, E. Heyman, R. Kastner, and R. W. Ziolkowski, Hybrid ray-FDTD moving window approach to pulse propagation, *J. Comput. Phys.* **138**, 480 (1997).
19. Y. Liu, Fourier analysis of numerical algorithms for the Maxwell's equations, *J. Comput. Phys.* **124**, 396 (1996); R. Janaswamy and Y. Liu, An unstaggered colocated finite-difference scheme for solving time-domain Maxwell's equations in curvilinear coordinates, *IEEE Trans. Antennas Propag.* **45**, 1584 (1997).
20. T. A. Driscoll and B. Fornberg, Note on nonsymmetric finite differences for Maxwell's equations, *J. Comput. Phys.* **161**, 723 (2000).
21. G. P. Agrawal, *Nonlinear Fiber Optics*, 2nd ed. (Academic Press, San Diego, 1995).
22. J. R. Taylor, *Optical Solitons, Theory and Experiment* (Cambridge Univ. Press, England, 1992).
23. L. Gilles, H. Bachiri, and L. Vázquez, Evolution of higher-order bright solitons in a nonlinear medium with memory, *Phys. Rev. E* **57**, 6079 (1998).
24. J. Satsuma and N. Yajima, Initial value problems of one-dimensional self-modulation of nonlinear waves in dispersive media, *Prog. Theor. Phys. (Jpn.)* **55**(suppl.), 284 (1974); F. Abdullaev, S. Darmanyan, and P. Khabibullaev, *Optical Solitons* (Springer-Verlag, Berlin, 1993).
25. J. B. Schneider and C. L. Wagner, FDTD dispersion revisited: Faster-than-light propagation, *IEEE Microwave Guided Wave Lett.* **9**, 54 (1999).
26. K. E. Oughstun and S. Shen, Velocity of energy transport for a time-harmonic field in a multiple-resonance Lorentz medium, *J. Opt. Soc. Am. B* **5**, 2395 (1988).
27. P. N. Butcher and D. Cotter, *The Elements of Nonlinear Optics* (Cambridge Univ. Press, England, 1990).
28. R. Richtmyer and K. Morton, *Difference Methods for Initial-Value Problems* (Wiley, New York, 1967).
29. T. Taniuti, Reductive perturbation method and far fields of wave equations, *Prog. Theor. Phys. (Jpn.)*, **55**(suppl.), 1 (1974); Y. Kodama and A. Hasegawa, Nonlinear pulse propagation in a monomode dielectric guide, *IEEE J. Quant. Electron.* **23**, 510 (1987); T. Taniuti and K. Nishihara, *Nonlinear Waves* (Pitman, London, 1983).
30. K. J. Blow and D. Wood, Theoretical description of transient stimulated Raman scattering in optical fibers, *IEEE J. Quant. Electron.* **25**, 2665 (1989).

31. P. G. Petropoulos, L. Zhao, and A. Cangellaris, A reflectionless sponge layer absorbing boundary condition for the solution of Maxwell's equations with high-order staggered finite difference schemes, *J. Comput. Phys.* **139**, 184 (1998).
32. A. Yefet and P. G. Petropoulos, A non-dissipative staggered fourth-order accurate explicit finite difference scheme for the time-domain Maxwell's equations, submitted for publication.
33. M. H. Carpenter, D. Gottlieb, and S. Abarbanel, Stable and accurate boundary treatments for compact high-order finite-difference schemes, *Appl. Numer. Anal.* **12**, 55 (1993).